

## Article

# Anaerobic Microscopic Analysis of Ferrous Saponite and Its Sensitivity to Oxidation by Earth's Air: Lessons Learned for Analysis of Returned Samples from Mars and Carbonaceous Asteroids

Natsumi Noda <sup>1,2,\*</sup>, Shohei Yamashita <sup>3</sup>, Yoshio Takahashi <sup>2,3</sup>, Megumi Matsumoto <sup>4</sup>, Yuma Enokido <sup>4</sup>, Kana Amano <sup>4</sup>, Takahiro Kawai <sup>2</sup>, Hiroshi Sakuma <sup>5</sup>, Keisuke Fukushi <sup>6</sup>, Yasuhito Sekine <sup>1,6</sup> and Tomoki Nakamura <sup>4</sup>

- <sup>1</sup> Earth-Life Science Institute (ELSI), Tokyo Institute of Technology, 2-12-1 Ookayama, Meguro-ku, Tokyo 152-8550, Japan; sekine@elsi.jp
  - <sup>2</sup> Department of Earth and Planetary Science, The University of Tokyo, 7-3-1 Hongo, Bunkyo-ku, Tokyo 113-0033, Japan; ytakaha@eps.s.u-tokyo.ac.jp (Y.T.); taka\_k@eps.s.u-tokyo.ac.jp (T.K.)
  - <sup>3</sup> Institute of Materials Structure Science Photon Factory, High Energy Accelerator Research Organization (KEK), 1-1 Oho, Tsukuba 305-0801, Japan; yamasho@post.kek.jp
  - <sup>4</sup> Division of Earth and Planetary Materials Science, Tohoku University, 6-3 Aramaki Aza-Aoba, Aoba Ward, Sendai 980-8578, Japan; m\_matsumoto@tohoku.ac.jp (M.M.); yuma.enokido.r8@dc.tohoku.ac.jp (Y.E.); amakana@dc.tohoku.ac.jp (K.A.); tomoki.nakamura.a8@tohoku.ac.jp (T.N.)
  - <sup>5</sup> National Institute for Materials Science, 1-1 Namiki, Tsukuba 305-0044, Japan; SAKUMA.Hiroshi@nims.go.jp
  - <sup>6</sup> Institute of Nature and Environmental Technology, Kanazawa University, Kakuma, Kanazawa 920-1192, Japan; fukushi@staff.kanazawa-u.ac.jp
- \* Correspondence: natsumi@elsi.jp



**Citation:** Noda, N.; Yamashita, S.; Takahashi, Y.; Matsumoto, M.; Enokido, Y.; Amano, K.; Kawai, T.; Sakuma, H.; Fukushi, K.; Sekine, Y.; et al. Anaerobic Microscopic Analysis of Ferrous Saponite and its Sensitivity to Oxidation by Earth's Air: Lessons Learned for Analysis of Returned Samples from Mars and Carbonaceous Asteroids. *Minerals* **2021**, *11*, 1244. <https://doi.org/10.3390/min1111244>

Academic Editor: Kattathu J. Mathew

Received: 26 September 2021

Accepted: 3 November 2021

Published: 9 November 2021

**Publisher's Note:** MDPI stays neutral with regard to jurisdictional claims in published maps and institutional affiliations.



**Copyright:** © 2021 by the authors. Licensee MDPI, Basel, Switzerland. This article is an open access article distributed under the terms and conditions of the Creative Commons Attribution (CC BY) license (<https://creativecommons.org/licenses/by/4.0/>).

**Abstract:** Ferrous saponite is a secondary mineral that can be used to reveal the redox state of past aqueous environments on Mars. In mineralogical analyses for ferrous saponite formed in laboratory simulations or contained in future returned samples from Mars, its oxidation by the Earth's air could be problematic due to the high redox sensitivity. Here, we performed micro X-ray diffraction and scanning transmission X-ray microscopy analyses for a single particle of synthesized ferrous saponite without any exposure to air. The sample was reanalyzed after air exposure for 10–18 h to assess the adequacy of our anoxic preparation/measurement methods and the impacts of air on the sample. We found that the crystal structures agreed with ferrous saponite, both before and after air exposure; however, ferrous iron in saponite was partially oxidized, at least until 0.1–1  $\mu\text{m}$  from the surface, after air exposure at the submicron scale, forming micro-vein-like Fe(III)-rich features. Together with our results of infrared spectroscopy of ferrous saponite, we showed that oxidation of octahedral iron occurred rapidly and heterogeneously, even in a short time of air exposure without any structural rearrangement. Since ferrous saponite is expected to exist on carbonaceous asteroids and icy dwarf planets, our methodology is also applicable to mineralogical studies of samples returned from these bodies.

**Keywords:** Fe-bearing clay minerals; ferrous saponite; redox chemistry; micro XRD; STXM; XANES; Mars

## 1. Introduction

Knowledge of the redox evolution of aqueous environments on Mars is critical to understanding geochemical cycles and habitability (e.g., [1,2]). Sedimentary records revealed by Mars rovers, their interpretations based on experiments and modeling, and Martian meteorite analyses show that the redox states of aqueous environments would have dramatically changed on early Mars depending on time and locations (e.g., [3–11]).

Among secondary minerals on Mars, iron-bearing smectite is one of the promising mineralogical phases to assess redox states and pH of paleo-environments [8,12,13]. The global presence of smectite on Mars was reported by orbital observations using visible/near-infrared (VNIR) instruments, such as OMEGA (Observatoire pour la Minéralogie, l'Eau, les Glaces et l'Activité) and CRISM (Compact Reconnaissance Imaging Spectrometer) onboard Mars Express and Mars Reconnaissance Orbiter, respectively [14–18]. The widespread clay mineral-bearing outcrops, especially within Noachian terrains, are indicators of occurrence of water-rock reactions, and would provide information about the geochemical and hydrological cycles at the time of formation (e.g., [14]). To characterize the mineralogy and chemistry of Martian smectite, previous studies used infrared absorption at a wavelength around 2–3  $\mu\text{m}$  associated with the vibration between cation filling the octahedral site and structural OH (e.g., [19]). The global distribution of Martian smectite shows a variation in both mineralogical groups (tri- to di-octahedral) and octahedral cation composition (Mg-rich to Fe-rich) [14,20]. The observed smectite with the absorption band at wavelength of 2.30  $\mu\text{m}$  is assigned to be ferric (Fe(III)) dioctahedral smectite, which requires oxidizing aqueous environments [20]. Recent experiments argue that later oxidation of trioctahedral  $\text{Fe}^{2+}$ -bearing smectite, hereafter called ferrous saponite, can explain the absorption band at  $\sim 2.30 \mu\text{m}$  [12].

Ferrous saponite is a secondary mineral formed through water-rock reactions under anoxic and alkaline conditions. Considering the mafic crust of Mars that contains reduced iron (Fe(II)) [21], ferrous saponite occurrence would be widespread on Mars through crustal aqueous alterations [14]. Substantial amounts of ferrous saponite may also have been generated through hydrothermal alteration of crust in the earliest stage of planetary evolution during magma ocean cooling [22]. The existence of Fe-rich saponite within sedimentary rocks is indicated by the Mars Science Laboratory Rover, Curiosity, using an X-ray diffraction (XRD) spectrometer, CheMin [23]. The 02l diffraction peaks corresponding to 4.59  $\text{\AA}$  for the John Klein and Cumberland drilling samples were attributed to ferrian saponite, which has a trioctahedral sheet dominantly filled with  $\text{Fe}^{3+}$  [23,24]. Combined with the experimental results, it was suggested that ferrous saponite is the precursor of the detected ferrian saponite [12,24].

Although ferrous saponite also occurs on Earth in anoxic alkaline aqueous environments [25,26], its sensitivity against oxidation by  $\text{O}_2$  in the atmosphere has made it difficult to study its mineralogy and geochemistry in natural samples. Instead, synthesized ferrous saponite has been used for characterization of its spectroscopic properties [27,28]. Ferrous saponite with various octahedral cation compositions ( $\text{Fe}^{2+}$ ,  $\text{Fe}^{3+}$ , Mg, and Al) has been analyzed using multiple techniques, such as infrared spectroscopy [27,28]. These series of analyses demonstrated that a 2–3  $\mu\text{m}$  absorption position can be used to constrain the octahedral cation composition and the oxidation state of Fe [27,28]. Such spectroscopic catalogs have improved the orbital capabilities to identify ferrous saponite and its possible oxidation products (e.g., ferrian saponite). To further interpret the formation and alteration environments of ferrous saponite on early Mars, mineralogical and chemical analyses of laboratory simulants that went through the similar environments would be required (e.g., [12,29]). Considering the redox sensitivity of ferrous saponite, laboratory experiments using ferrous saponite may suffer from oxidation by the Earth's air during experimental and analytical procedures. For instance, previous work estimated different oxidation states of ferrous saponite based on the two different analyses (X-ray absorption fine structure (XAFS) and Mössbauer spectroscopy) [12]. Thus, the differences between the analytical procedures may have been caused by different degrees of air exposure during the measurements [10]. Thereby, evaluation of oxidation of ferrous saponite by air under controlled conditions is necessary to interpret results of analyses of laboratory simulants and future returned samples from Mars (e.g., MSR: Mars Sample Return mission [30]) and Martian moons (e.g., MMX: Martian Moons eXploration mission [31]).

Ferrous saponite formation is expected not only on early Mars and Earth, but also on other volatile-rich small bodies, such as icy satellites, icy dwarf planets, and carbonaceous

asteroids [32–38]. The demand for analyzing ferrous saponite is expanding into mineralogical and geochemical analyses for returned samples from carbonaceous asteroids (e.g., the Hayabusa 2 and OSIRIS-REx missions) and their laboratory simulants [39–41]. To analyze samples composed of multiple phases (e.g., a serpentine/saponite mixed layer) and with limited amounts, microscopic analytical techniques using synchrotron radiation are effective (e.g., [42]). However, no previous study has demonstrated microscopic analysis to assess the effects of oxidation of ferrous saponite.

Here, we demonstrated microscopic analyses of synthesized ferrous saponite without any air exposure using micro XRD and scanning transmission X-ray microscopy (STXM). The preparation, installation, and measurement of the samples were carried out under anaerobic conditions in both analyses. X-ray absorption spectroscopy and infrared reflectance spectroscopy were used to characterize bulk powder samples under anaerobic conditions with the least air exposure (<3 min) during sample setting. In addition, we repeated all analyses after exposure of the same ferrous saponite samples to ambient air for about half a day (10–18 h). There were two objectives for this parallel analysis: One was to confirm the suppressed contribution of air in anaerobic preparation/measurement of ferrous saponite, and the other was to assess how the air exposure with the timescale of sample preparation impacted the analytical results.

## 2. Materials and Methods

### 2.1. Materials: Synthesis of Ferrous Saponite

The ferrous saponite sample in this study was synthesized with a sol-gel method modified from previous work [27,43,44]. To prevent oxidation of iron by atmospheric oxygen, the synthesis was done in an acrylic glovebox connected to a deoxygenation system (SiOC-2000 GB; STLab Co., Ibaraki, Japan) [45,46]. The concentration of oxygen (O<sub>2</sub>) in the glovebox was kept below 1 ppb during the experimental procedures by purging argon (Ar) gas and circulation through the deoxygenation system. Since dissolved oxygen (DO) also causes oxidation of iron, ultrapure water used for all following procedures was deoxidized before use. To reduce DO to lower than 0.01 ppm, 0.5 L of Milli-Q water was bubbled with Ar gas (>99.999 vol.%, Suzuki Shokan, Japan) at 2.8 L/min for 3 h in the glovebox.

A stock solution was prepared from 4 types of salt reagents: iron (II) sulfate heptahydrate, magnesium chloride hexahydrate, aluminum (III) chloride hexahydrate (Guaranteed Reagent, Wako Pure Chemical Industries, Ltd., Osaka, Japan), and sodium orthosilicate (practical grade, Nacalai Tesque, Inc., Kyoto, Japan) (Table 1). The proportions were determined to stoichiometry representing the target saponite composition with Mg: Fe<sup>2+</sup> = 1:1 for octahedral and Si:Al = 7:1 for tetrahedral composition; i.e., the ideal half-cell formula described as Na(Mg<sub>1.5</sub>Fe<sup>2+</sup><sub>1.5</sub>)(Si<sub>3.5</sub>Al<sub>0.5</sub>)O<sub>10</sub>(OH)<sub>2</sub>. The homogenized salts were dissolved using a magnetic stirrer to 50 mL of 0.5 wt. % sodium hydrosulfite solution prepared from deoxidized ultrapure water and sodium hydrosulfite (practical grade, Wako Pure Chemical Industries, Ltd., Osaka, Japan). After stirring for >15 min until the salts dissolved, the stock solution was sealed within PTFE (polytetrafluoroethylene) containers that were set in decomposition vessels (HU-100, San-Ai Kagaku Co., LTD., Aichi, Japan). The decomposition vessels could withstand temperatures below 230 °C and pressure below 15 MPa by covering the sealed PTFE container with a stainless steel (SUS) cylinder. The sealed containers of stock solution were enclosed in SUS cylinders and kept at 180 °C for ~160 h in an electric oven.

**Table 1.** The composition of the stock solution prepared for the ferrous saponite synthesis experiment in this study. The standard errors are shown in parentheses.

Reagent	Molecular Equation	Concentration (mmol/kg)
Sodium orthosilicate	$\text{Na}_4\text{SiO}_4$	90.0 (0.2)
Iron (II) sulfate heptahydrate	$\text{FeSO}_4 \cdot 7\text{H}_2\text{O}$	38.6 (0.1)
Magnesium chloride hexahydrate	$\text{MgCl}_2 \cdot 6\text{H}_2\text{O}$	38.7 (0.4)
Aluminum (III) chloride hexahydrate	$\text{AlCl}_3 \cdot 6\text{H}_2\text{O}$	12.9 (0.1)

After the hydrothermal treatments, the aged solutions were transferred to polycarbonate centrifuge tubes in the glovebox. The precipitate was collected by centrifuging at 3500 rpm for 30 min, followed by two cycles of rinsing to remove remaining chloride salts. The rinsing was carried out by replacing the supernatant with ultrapure water to form a suspension and centrifuging again. Although the samples were centrifuged outside the glovebox, the centrifuge tube was sealed with a screwed cap with PTFE tape in the glovebox to prevent the inflow of air. The precipitate was then dried by vacuum (<1 mbar) for 2 days in a chamber directly connected to the glovebox. The dried ferrous saponite was powdered using an agate mortar and was subsequently sealed together with an oxygen absorber in the glovebox. The sealed samples were transported to the synchrotron radiation facility for the analyses (see Section 2.2).

## 2.2. Methods of Analysis and Air Exposure

### 2.2.1. Synchrotron-Radiation-Based Micro XRD

To characterize the mineralogical structure of the synthesized ferrous saponite, we performed micro XRD analysis of a saponite particle at beamline BL-3A in the Photon Factory, Institute of Materials Structure Science, KEK, Japan. Following a micro XRD measurement of a single particle, an STXM analysis was performed for the same sample without air exposure.

A ferrous saponite particle of 100  $\mu\text{m}$  in size, coated with fine Si particles, was mounted in a Gandolfi camera in a nitrogen-substituted glove bag with an atmospheric pressure of 1 bar. Monitored  $\text{O}_2$  and humidity in the glove bag were kept at <0.01% and <1%, respectively. The saponite particle was stored under dry conditions for about one month in a nitrogen ( $\text{N}_2$ )-filled glove box at Tohoku University. The camera was evacuated with a dry scroll pump, and the sample was irradiated with X-rays at a wavelength of  $2.1680 \pm 0.0008$  angstroms ( $\text{\AA}$ ) for 15 min to obtain a powder XRD pattern. To observe the structural changes caused by air exposure, XRD experiments were performed another three times; that is, the mounted ferrous saponite particle was exposed to ambient air for about 2 h, 4.5 h, and 10 h. The XRD patterns were obtained with irradiation times of 15 min. Thus, the same particle was analyzed four times with the same camera setting and the same exposure time, so that the difference in the XRD patterns was ascribed to have occurred by oxidation and/or hydration in the air. The obtained XRD pattern was developed by the imaging plate (IP) reader (Typhoon FLA 7000; GE Healthcare) and was calibrated with Si diffraction using the analysis software GanCon2, developed by Nakamura T.

### 2.2.2. XANES Spectra

Following the micro XRD experiment for the ferrous saponite particle without air exposure, the same sample was thinned with the focused ion beam (FIB) system (SMI3200, Hitachi High-Tech Science Co., Ltd., Tokyo, Japan) for STXM analysis in an anaerobic atmosphere. Helium (He) gas (G1 grade, He > 99.99995%) was continuously flowed at a rate of 3 L/min into a glove bag attached to the FIB system. The sample sealed under an anaerobic condition was transferred into the glove bag. Nitrogen gas (industrial grade,  $\text{N}_2$  > 99.99%) was also connected to the FIB system to replace the gas that contacts the

sample during the venting process. Monitored O<sub>2</sub> in the glove bag was less than 1.0%. A section of the ferrous saponite particle was cut with an ion beam, picked up on a molybdenum grid, and fixed by carbon deposition. After these procedures, a thinning treatment was performed to create parts with thicknesses of ca. 250 nm. This thickness is suited for scanning the Fe L-edge of carbonaceous chondrites by STXM. The prepared sample was sealed with an oxygen absorber and stored in a glovebox, where O<sub>2</sub> was below 10 ppm.

The STXM technique enabled us to conduct X-ray absorption near-edge structure (XANES) mappings with a high spatial resolution of approximately 30 nm by applying a Fresnel zone plate. The STXM measurements of the FIB thin section sample were performed at beamline BL-19A in the Photon Factory. The sealed FIB thin section sample was opened and installed on the measurement stage in a customized glovebox docked directly above the compact STXM chamber [47]. The glovebox was purged with Ar gas (G1 grade, Ar > 99.99994%) at an atmospheric pressure of 1 bar during the sample installation. The level of O<sub>2</sub> (LD-450-C, Toray Engineering Co., Ltd., Tokyo, Japan) and dew point (SP-323-4-A2, UINICS Co., Ltd.) were continuously monitored and kept at several ppm and −60 °C, respectively. The STXM chamber was closed and then filled with He gas (G1 grade, He > 99.99995%) at 0.1 bar during the measurements. After the focus was adjusted to the section sample, XANES mappings were carried out around the Fe L-edge (700–732 eV). An area of 1.5 μm × 2.4 μm was raster-scanned with a 10 ms dwell time per 50 nm × 50 nm sized pixel. Following the experiment without air exposure, the analyzed sample was taken out and placed in ambient air for about 18 h. The STXM measurement for the air-exposed sample was performed with the same procedures, except for a wider area of 2.5 μm × 3.2 μm, including the area previously analyzed. The obtained stack images were converted to optical density to extract the XANES spectra using the analysis software aXis2000 [48].

The XANES spectra of the bulk ferrous saponite powder and reference materials were obtained at Beamline 19B in the Photon Factory. We used commercially purchased biotite (K(Mg, Fe<sup>2+</sup>)<sub>3</sub>(Al, Fe<sup>3+</sup>)Si<sub>3</sub>O<sub>10</sub>(OH, F)<sub>2</sub>; #8. ED. 120-1, Nichika Inc., Kyoto, Japan; the Fe<sup>3+</sup>/ΣFe ratio was estimated at 2.8% based on the below potassium dichromate titration method under N<sub>2</sub> atmosphere) as a reference of phyllosilicate that composed ferrous iron in an octahedral sheet with a low Fe<sup>3+</sup>/ΣFe ratio. We also used commercially purchased montmorillonite ((Na<sub>0.42</sub>K<sub>0.008</sub>Ca<sub>0.068</sub>)(Al<sub>1.56</sub>Mg<sub>0.31</sub>Fe<sup>3+</sup><sub>0.09</sub>Fe<sup>2+</sup><sub>0.01</sub>)(Si<sub>3.91</sub>Al<sub>0.09</sub>)O<sub>10</sub>OH<sub>2</sub> [49]; Kunipia-F, Kunimine Industries Co., LTD., Tokyo, Japan) as a reference of phyllosilicates that contained ferric iron in an octahedral sheet with a high Fe<sup>3+</sup>/ΣFe ratio of 90%. Approximately 100 μg of sample powder was mounted on a copper plate and was then evacuated to 10<sup>−5</sup> Pa immediately after the plate was placed at measurement stage. The duration of air exposure during sample preparation was shorter than 3 min. The XANES spectra in electron yield mode around the Fe L-edge (700–740 eV) were collected for each sample with an energy step of 0.1 eV and a dwell time of 100 ms per step. The air was introduced to the sample chamber after the first measurement. Then, the same measurement was performed after 11 h of air exposure. The obtained XANES spectra were calibrated with absorption edge *E*<sub>0</sub> and normalized using the analysis software Athena ver. 0.9.26 [50].

### 2.2.3. IR Spectroscopy

We performed Fourier-transform infrared spectroscopy (FTIR) of the synthesized saponite sample with two types of methods: In one, a diffuse reflection method was employed for the powder sample mixed with KBr powder in the mid-infrared (MIR) and near-infrared (NIR) region. In the other, a reflection method was used for the powder sample enclosed in an air-tight cell in the visible to near-infrared (VNIR) region.

MIR and NIR spectroscopy (Frontier, PerkinElmer Japan Co., Ltd., Kanagawa, Japan) was performed with the diffuse reflection method for the powder saponite sample mixed with pure KBr powder (PIKE Technologies Inc.). To eliminate hydration and oxidation during the measurements, pure N<sub>2</sub> gas (G1 grade, N<sub>2</sub> > 99.99995%) was purged in the

sample room throughout the measurements. For the measurement without air exposure, ferrous saponite powder was mixed with KBr powder using an agate mortar immediately before the measurements (~20 min) under anoxic conditions ( $O_2 < 1$  ppb). The mixed powder was exposed to air for ~15 s during the sample installation. As for the measurement after air exposure, ferrous saponite powder was placed under ambient air for 14 h and 1250 h (~50 days). These exposed samples were mixed with KBr powder for FT-MIR/NIR analyses. For the sample preparation, the mixing ratios of saponite were approximately 2 wt. % relative to the KBr powder. The KBr powder without saponite was also prepared and measured as background in the measurements. MIR spectra were obtained for the wavenumber ranges of 4000–400  $cm^{-1}$  with resolutions of 1  $cm^{-1}$ . NIR spectra were obtained in the wavelength range of 0.7–5  $\mu m$  at a resolution of 0.00035  $\mu m$ . Each sample was measured 2–3 times using remixed powder. The averaged spectra were smoothed by the 25-point moving average, followed by removal of continuum components estimated by the 1001-point moving average from NIR spectra. Both the NIR and MIR absorption features of the sample could provide insights into changes in the mineralogical structure and/or cation (i.e.,  $Fe^{2+}$  vs.  $Fe^{3+}$ ) composition of the saponite samples due to the air exposure (see Section 3.3 for details). For comparison, infrared spectra of commercially purchased Mg saponite ( $Na_{0.33}Mg_3(Si_{3.67}Al_{0.33})O_{10}OH_2$ ; Sumecton-SA, Kunimine Industries Co., LTD., Tokyo, Japan), natural nontronite (Clay Mineral Society source clay, sample ID: NG-1) ( $(Al_{0.36}Fe_{1.61}Mg_{0.03})(Si_{3.56}Al_{0.13}Fe_{0.31})O_{10}OH_2$  [51]), natural ferric smectite (Clay Mineral Society source clay, sample ID: SWa-1) ( $(Al_{0.55}Fe_{1.31}Mg_{0.13})(Si_{3.70}Al_{0.30})O_{10}OH_2$  [51]), and commercially purchased magnetite (Wako Pure Chemical Industries, Ltd.) were acquired.

VNIR reflectance spectroscopy (VERTEX 70v, Bruker Corp.) of the powder saponite sample with a wavelength range from 0.4  $\mu m$  to 8  $\mu m$  was also performed before and after air exposure. The incidence and emission angles were  $30^\circ$  and  $0^\circ$ , respectively. Approximately 50 mg of unexposed saponite powder was taken out from the sealed vial and put into an air-tight cell with a  $CaF_2$  window in a  $N_2$ -purged glove box in which  $O_2$  was  $< 0.1\%$  and humidity was  $< 1\%$ . Reflectance standard slabs, such as Labsphere Spectralon (99% reflectance) and Infragold, were also enclosed along with the sample to remove effects of the optical window. The cell was put into the spectrometer and vacuumed down to 3 mbar, while the inside of the cell was at the atmospheric pressure of nitrogen. After the measurements, the powder sample was exposed to air for 12 h in the laboratory (we opened the  $CaF_2$  window, and the sample stayed in the cell). The exposed sample was analyzed under the same conditions as that of the unexposed sample, except this time the cell was filled with atmosphere. The spectral resolution was 32  $cm^{-1}$  at visible wavelengths and 4  $cm^{-1}$  at infrared wavelengths. The spectra were obtained from the central 4 mm diameter area of the powdered sample.

### 3. Results

#### 3.1. XRD Pattern

The XRD pattern of our synthesized sample without air exposure confirmed the analyzed particle to be ferrous smectite, together with trace amounts of magnetite or maghemite (Figure 1a). The 001, 021, and 060 diffraction peaks attributed to smectite were observed at  $2\theta = 11.0^\circ \pm 0.2^\circ$ ,  $27.4^\circ \pm 0.2^\circ$ , and  $89.5^\circ \pm 0.2^\circ$ , respectively (Figure 1b,c). The peak position of broad 001 reflectance corresponded to the basal interlayer spacing of  $11.3 \text{ \AA} \pm 0.2 \text{ \AA}$ . This interlayer spacing was consistent with the expanded 2:1 layered structure of smectite. Compared to those of synthesized ferrous saponite reported previously (14–17  $\text{\AA}$  [27,28]), the low value of interlayer spacing of our sample was attributed to the interlayer cations not being exchanged to  $Ca^{2+}$ , but remaining occupied by  $Na^+$  [44]. The 060 reflection of  $1.540 \text{ \AA} \pm 0.003 \text{ \AA}$  corresponded to the b unit cell parameter of  $9.24 \pm 0.02$ , consistent with a trioctahedral structure [27]. The 021 reflection of  $4.58 \text{ \AA} \pm 0.03 \text{ \AA}$  agreed with that of ferrous saponite reported in earlier work [27,28] and Griffith ferrian saponite [24], which strongly supported our synthesized saponite having a trioctahedral structure.

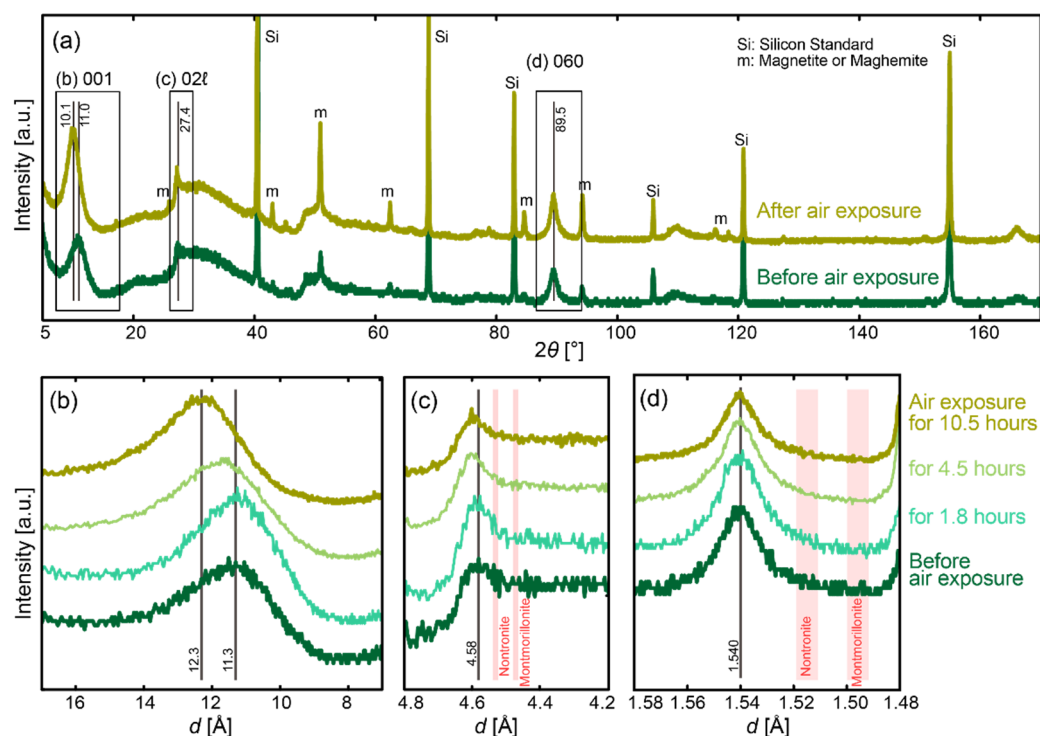


**Figure 1.** (a) XRD patterns obtained before and after air exposure (10.5 h). The squares show the region expanded in panels (b–d), which show close-up XRD patterns obtained before and after 1.8 h, 4.5 h and 10.5 h of air exposure. The black vertical lines show the peak positions of dioctahedral saponite (see the main text). The red vertical lines in the panels (c,d) show the peak positions of dioctahedral smectites for comparison. Each pattern is scaled and offset for clarity.

The XRD patterns of saponite obtained after air exposures of a few to 10 h showed no significant differences in the diffraction patterns from those without air exposure, except for the 001 diffraction peak position. Figure 1a,b show that the 001 diffraction peak position gradually decreased with the time of air exposure (e.g.,  $2\theta = 10.1^\circ \pm 0.2^\circ$  after 10.5 h of air exposure), corresponding to an increase in interlayer spacing to  $12.3 \text{ \AA} \pm 0.2 \text{ \AA}$ . This shift in interlayer spacing could have been caused by hydration of interlayer cations during air exposure, although the XRD measurements were conducted in an evacuated camera where pressure  $<10^{-2}$  Pa. In the present study, the sample preparation of the unexposed sample was performed in a globe box in which the humidity was 1% or less. Then, the air exposure was performed with ambient air with a relative humidity (RH) of approximately 50%. An increase in interlayer spacing was reported in response to an increase in RH from ~20% to 40% for Na-montmorillonite, due to transformation to a one-molecular-layer hydration state [52]. Assuming similar hydration would have occurred for our saponite, a sample with a longer exposure time may have suffered from more hydration of interlayers, possibly causing the observed increase in interlayer spacing as a function of exposure time. Our results showed that the XRD peak due to the 02l reflection at  $4.58 \text{ \AA}$  was unchanged throughout the experiments (Figure 1c). If any change from trioctahedral to dioctahedral structures occurred in our saponite upon air exposure, the XRD peak due to the 02l reflection should have shifted from  $4.58 \text{ \AA}$  to  $4.50 \text{ \AA}$ , which is characteristic of dioctahedral smectite, such as montmorillonite and nontronite [23,53]. Therefore, no shift in the 02l d-spacing strongly suggested that the trioctahedral structure was largely unchanged upon air exposure. The uniform 060 reflection also indicated that there was no structural change from a trioctahedral to dioctahedral sheet due to air exposure (Figure 1d). If any change to a dioctahedral structure occurred, the XRD peak at  $1.540 \text{ \AA}$  should have shifted toward lower values.

### 3.2. XANES Spectra

#### 3.2.1. Bulk X-ray Absorption

To determine the oxidation state of Fe in synthesized ferrous saponite and its change through air exposure, XANES spectra at the Fe L-edge were collected for two types of samples: bulk powder and an FIB thin section (i.e., STXM). The bulk spectra of powder samples measured before and after 11 h of air exposure exhibited clear absorption features attributed to iron (Figure 2a). Both the spectra shared absorption features due to the presence of ferrous iron: a major peak at 707.4 eV and shoulders at 705.5 eV, 706.0 eV, and 708.0 eV. The sample after air exposure had the predominant absorption at 709.5 eV, which is the primary peak position due to the presence of ferric iron. To perform a linear combination fitting (LCF) for the obtained spectra using the analysis software Athena, the previous reference spectrum of magnetite obtained at the same beamline was used, in addition to those of phyllosilicates with ferrous or ferric iron (see Section 2.2.2). The fitting of the spectra explained the feature of the samples with a reliability factor (R-factor) of  $\sim 0.005$  (Figure 2b,c). The calculated weights of each reference are shown in Table 2. The  $\text{Fe}^{3+}/\Sigma\text{Fe}$  ratio in smectite increased from  $\sim 4\%$  to  $\sim 15\%$  within a short time (11 h) of air exposure, indicating effective oxidation of iron in smectite by air. Figure 2 also indicates that the relative abundance of magnetite may have increased after air exposure, which was consistent with the sharp peaks due to magnetite in the XRD pattern obtained after air exposure (Figure 1a). This would also be caused by oxidation of ferrous iron in smectite by air.

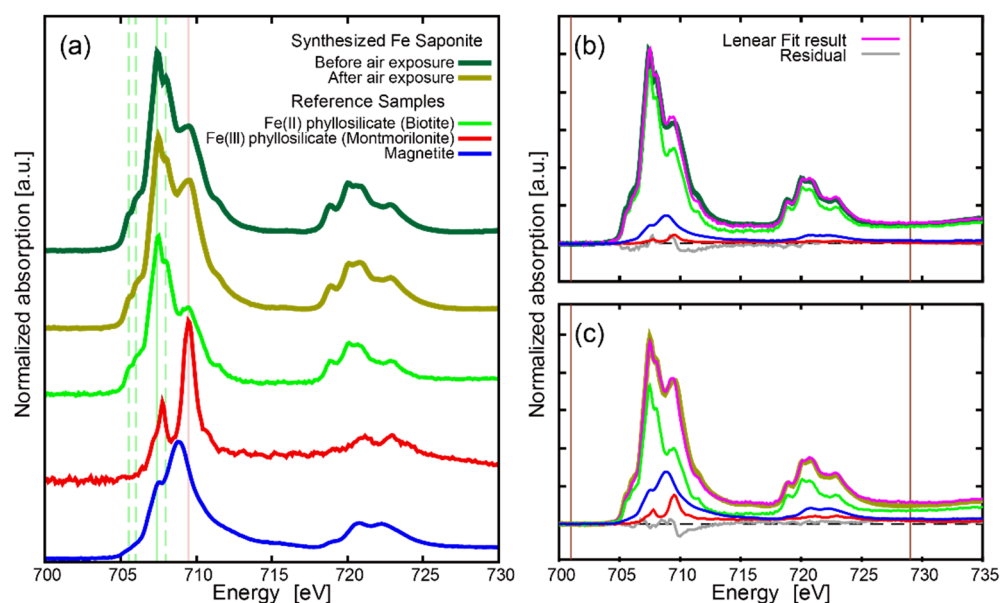


**Figure 2.** (a) Normalized XANES spectra around the Fe L-edge collected for bulk powder of synthesized ferrous saponite before and after air exposure with the reference samples, offset for clarity. Detailed descriptions about the reference samples are shown in the main text (Section 2.2.2). The X-ray energy was calibrated with an absorption edge of  $E_0 = 707.6$  eV. The vertical solid and dashed lines show the peak and shoulder energy positions, respectively, referred in the main text. (b,c) Results of linear combination fitting for the obtained spectra using reference data (b) before and (c) after air exposure. The pink curves in panels (b,c) show the sums of three reference components. The colors of the reference components in panels (b,c) are the same as those shown in panel (a). As the reference spectra of maghemite was unavailable, we could not rule out the possible presence of maghemite. The vertical brown lines show the lower and upper energy limits used for fitting. The horizontal dashed lines represent 0 in the absorption.

**Table 2.** Results of linear combination fitting of the Fe L-edge XANES spectra of the bulk powder of synthesized ferrous saponite collected before and after air exposure for 11 h. The calculated R-factor and the oxidation states of Fe ( $\text{Fe}^{3+}/\Sigma\text{Fe}$ ) in smectite are also shown. The  $\text{Fe}^{3+}/\Sigma\text{Fe}$  values in smectite were calculated in molar ratios based on those of the reference samples. The values in parentheses represent errors in the fitting.

Reference Sample	Before Air Exposure	After Air Exposure
$\text{Fe}^{2+}$ smectite	0.823 (0.008)	0.627 (0.008)
$\text{Fe}^{3+}$ smectite	0.041 (0.007)	0.129 (0.007)
Magnetite	0.137 (0.009)	0.243 (0.009)
R-factor	0.0053	0.0047
$\text{Fe}^{3+}/\Sigma\text{Fe}$ of smectite	0.043 (0.007)	0.154 (0.007)

### 3.2.2. STXM Analysis

XANES mapping around the Fe L-edge was performed for the FIB thin section samples using STXM. Figure 3a,b show a scanning ion microscope (SIM) image of the FIB thin section of the ferrous saponite particle. The broken squares in Figure 3a show the areas analyzed with STXM. The front view of the section shows an apparently uniform structure of the sample (Figure 3a). The bottom view of the section shows the uniform thickness for the analyzed area in between the molybdenum grid and the pillar structure (Figure 3b).

Figure 3c–f show the results of mapping of optical density at single X-ray energies. Panels (c) and (d) of Figure 3 represent the results before air exposure, whereas the panels (e) and (f) are those after air exposure for almost the same area of panels (c) and (d) (see panel (a) for the analyzed area). The difference in the optical density at an X-ray energy of 708.6 eV (Figure 3d,f) to 705.0 eV (Figure 3c,e) represented the difference in degree of absorption by iron in the samples. A comparison of Figure 3c,d indicated there was a difference in optical density due to the presence of iron in the top-right part of the analyzed area (hereafter, we will refer to this as the Fe-rich area). The area with low optical density in Figure 3c,d shows low levels of absorption due to iron (hereafter, we will refer to this area as the Fe-depleted area). A comparison of Figure 3e,f also showed that the distribution of Fe-rich/depleted area after air exposure agreed with that observed before air exposure (Figure 3c,d; see Section 4.2. for the formation mechanism). Both the left-end part in Figure 3c–f and the right-end part in Figure 3e,f are out of the thinned area with the FIB system (the dotted lines in the panel (b) correspond to those in the panels (c–f)). The typical XANES spectra of the Fe-rich and Fe-depleted areas are shown in Figure 3g. The XANES spectra showed that no significant X-ray absorption was featured at the Fe-depleted area, whereas there were clear absorption features due to iron in the Fe-rich area both before and after air exposure.

To further investigate the oxidation state of iron (i.e., ferrous vs. ferric) and the distribution in the Fe-rich/depleted area, singular value decomposition (SVD) mapping was conducted for both stack images (Figure 3h,i). We used four components (XANES spectra of ferrous saponite, ferric smectite, magnetite, and the Fe-depleted area) for fitting. Hereafter, we use the term ferric smectite for Fe(III)-rich smectite (ferric smectite does not represent nontronite). We displayed the results as a RGB color map using relative contributions by ferrous saponite (green), ferric smectite (red), and magnetite (blue). These three components were the same as those used for fitting the bulk spectra of the ferrous saponite powder before and after air exposure (Figure 2). The Fe-rich area was suggested to be composed mainly of ferrous saponite before air exposure (Figure 3h). On the other hand, the spectra after air exposure exhibited mixtures of ferric and ferrous iron in the Fe-rich area with spatial variation. In particular, the micro-vein-like structures (represented by the red color (ferric smectite) in Figure 3i) appeared in the Fe-rich area (Figure 3g), where ferrous saponite was predominant before air exposure (Figure 3h). These results strongly suggested that: (1) ferrous saponite was oxidized by air exposure even in a short time (i.e.,

half a day); and that (2) oxidation of ferrous saponite proceeded spatially heterogeneously within one ferrous saponite particle, forming micro-vein-like Fe(III)-rich structures.

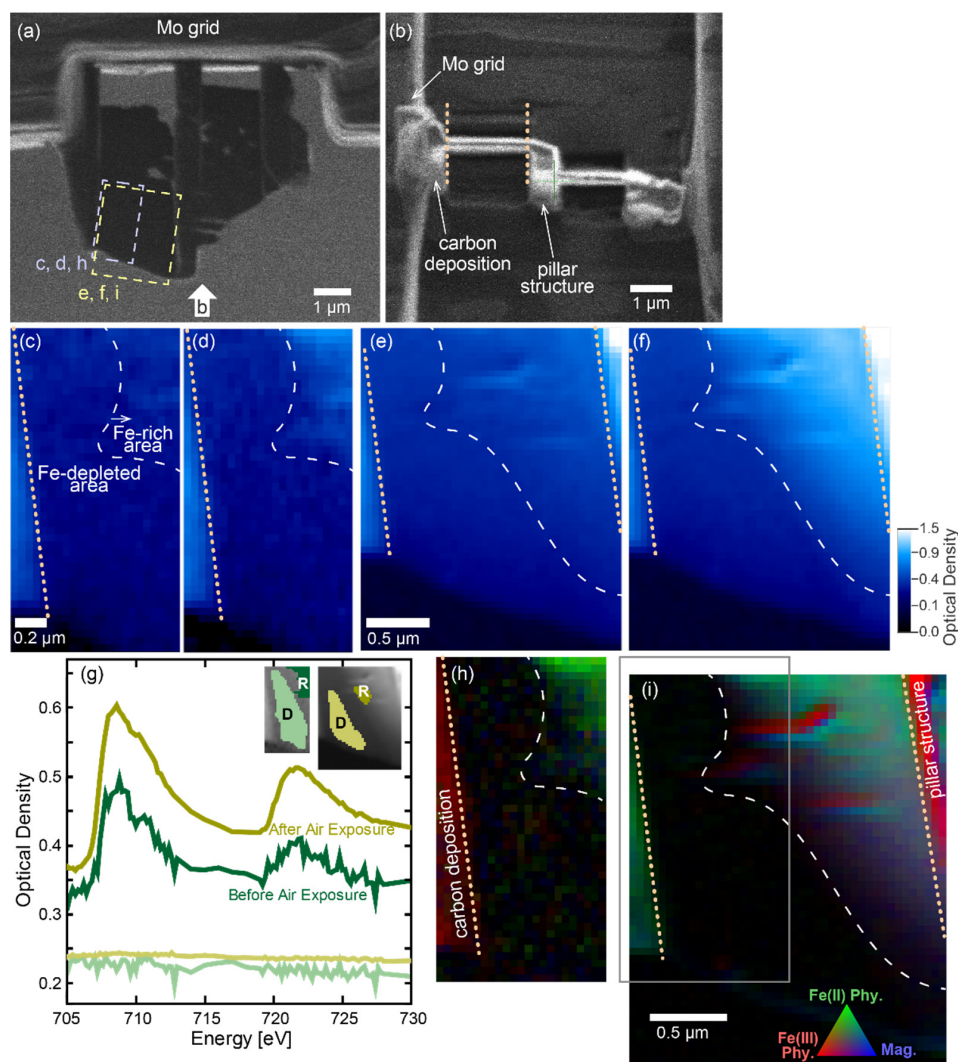


**Figure 3.** (a,b) Scanning ion microscope (SIM) image of the FIB thin section of the ferrous saponite particle. (a) SIM image view from the optical axis of STXM. The blue and yellow broken squares correspond to the areas scanned with STXM before (panels (c,d,h)) and after (panels (e,f,i)) air exposure, respectively. (b) SIM image view from the arrow direction in panel (a). The dotted lines show the left/right ends of the FIB thin section. (c–f) The optical density of X-rays collected before (panels (c,d)) and after (panels (e,f)) air exposure. The color represents optical density at 705.0 eV (no Fe absorption) (panels (c,e)) and at 708.6 eV (due to Fe(II) and Fe(III) absorption) (panels (d,f)). The orange dotted lines correspond to the range of thinned area shown in panel (b). The white broken curves represent the approximate boundary between the Fe-rich and Fe-depleted areas. (g) Typical XANES spectra at the Fe-rich and Fe-depleted areas. The areas used for extracting the spectra are shown in the top-right image with the same color for the index R (Fe-rich area) and index D (Fe-depleted area). (h,i) RGB map of the estimated composition using singular value decomposition (SVD) of XANES mapping before (panel (h)) and after (panel (i)) air exposure. Red, green, and blue represent the regions with presence of ferric smectite, ferrous saponite, and magnetite, respectively. The spectra of these three components were obtained by calibrating the reference spectra shown in Figure 2a using  $E_0$  to that of XANES spectra at the Fe-rich area shown in panel (g); that is,  $E_0 = 707.8$  eV for measurement before air exposure (panel (h)) and  $E_0 = 707.4$  eV for measurement after air exposure (panel (i)), respectively. The brightness and contrast were modified for clarity. The gray square in panel (i) corresponds to the scanned area before air exposure shown in panel (h).

### 3.3. IR Reflectance Spectroscopy

We performed FTIR spectroscopy of the synthesized ferrous smectite with both reflectance and diffuse reflectance methods independently, and obtained consistent results. We show the results of the diffuse reflectance method in the main text (see Appendix A for the results of the reflectance method). Figure 4 shows the MIR and NIR diffuse reflectance spectra before (spectrum B) and after air exposure of 14 h (spectrum A1) and 50 days (spectrum A2), together with those of the reference samples of Mg saponite Sumecton-SA, nontronite NG-1, ferric smectite SWa-1, and magnetite, for comparison. VNIR reflectance spectra before and after 12 h of air exposure are shown in Figure A1. All measured spectra exhibited the absorption features consistent with smectite. Namely, the absorptions caused by octahedral cation-OH vibration in bending ( $\delta M_n$ -OH), stretching ( $\nu M_n$ -OH), and a combination of both ( $\delta + \nu M_n$ -OH) modes were identified (Figure 4), where M represents octahedral cations; i.e., Mg,  $Fe^{2+}$ ,  $Fe^{3+}$ , or Al, and the suffix  $n$  represents the number of them.

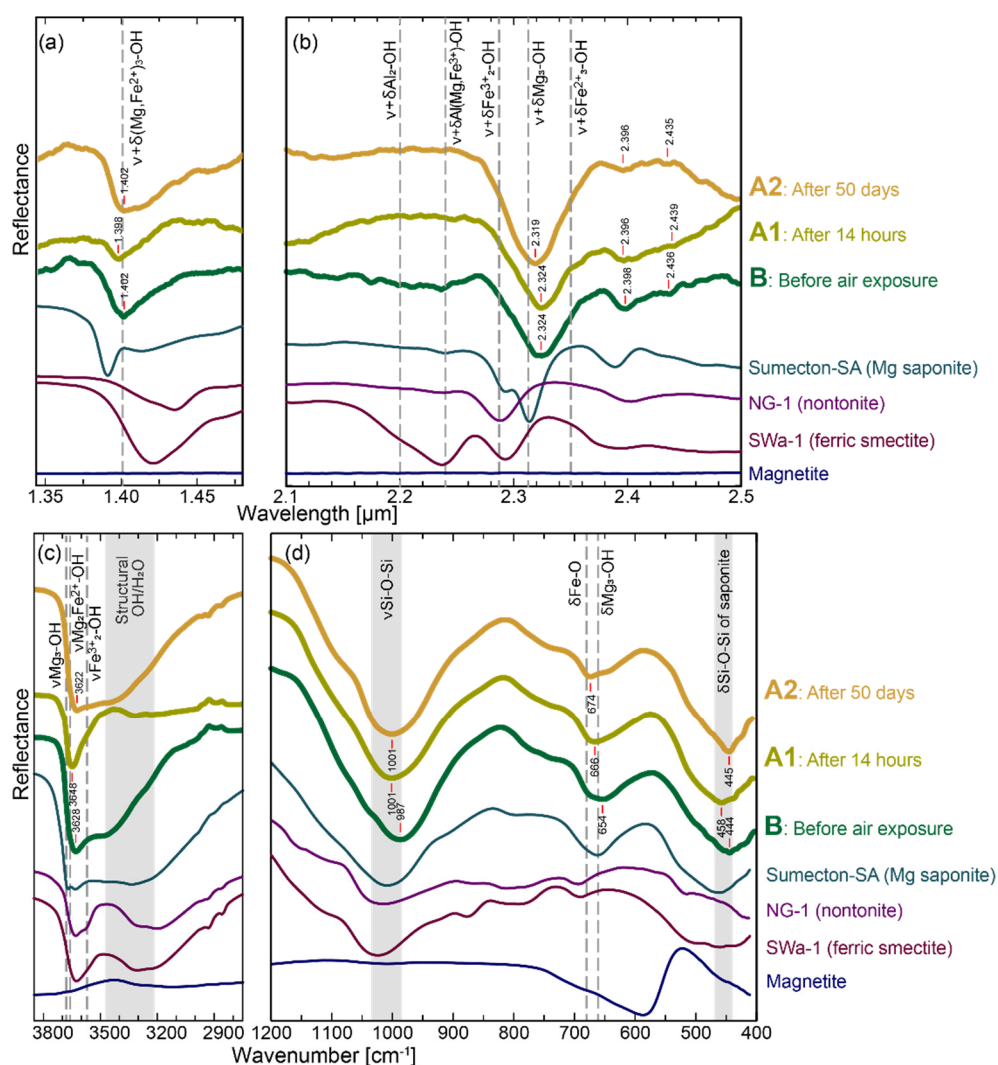


**Figure 4.** Results of NIR (a,b) and MIR (c,d) diffuse reflectance spectra of ferrous saponite before (spectrum B) and after air exposure for 14 h (spectrum A1) and 50 days (spectrum A2). The spectra of 4 reference samples are included for comparison. The spectra were scaled and offset after being smoothed for clarity. The numbers with red marks show the centers of the wavelength/wavenumber of absorptions. The gray vertical dashed lines and solid bars show the positions of sharp and broad absorption features, respectively, attributed to the vibrations (see the main text for details).

The absorptions due to  $\delta + \nu M_n\text{-OH}$  in the NIR region of 2.1–2.5  $\mu\text{m}$  (Figure 4b) are sensitive to the octahedral cation composition [20,24,27,28]. Our NIR spectra of ferrous saponite before and after air exposure exhibited neither strong Al-related absorption; e.g.,  $\delta + \nu \text{Al}_2\text{-OH}$  at 2.20  $\mu\text{m}$  and  $\delta + \nu \text{Al}_2(\text{Mg}, \text{Fe}^{3+})\text{-OH}$  at 2.23–2.25  $\mu\text{m}$  [28], nor strong  $\text{Fe}^{3+}$ -related absorption; e.g.,  $\delta + \nu \text{Fe}^{3+}_2\text{-OH}$  at 2.28–2.29  $\mu\text{m}$  [20,28]. The absence of these features supported the trioctahedral structure with low Al and  $\text{Fe}^{3+}$  contents in our samples, consistent with the results of the XRD analysis (Figure 1). The strong absorptions were observed at 2.32  $\mu\text{m}$ , which was in between the known peaks at 2.31  $\mu\text{m}$  due to  $\delta + \nu \text{Mg}_3\text{-OH}$  and at 2.35  $\mu\text{m}$  due to  $\delta + \nu \text{Fe}^{2+}_3\text{-OH}$ . The peak at 2.32  $\mu\text{m}$  was suggested to be attributed to  $\delta + \nu (\text{Mg}_2\text{Fe}^{2+})_3\text{-OH}$ , as seen in the synthesized ferrous trioctahedral smectites, samples D and H, in [27]. The synthesized ferrous trioctahedral smectite, sample P, in [28] also exhibited identical absorption at 2.31  $\mu\text{m}$ . These three previous smectite samples had high-Mg (>57 mol%) and low-Al (<13 mol%) octahedral cation compositions, similar to ours. Figure 4b shows a slight shift in the absorption center from 2.324  $\mu\text{m}$  in the spectra B and A1 (no/less oxidized saponite) to 2.319  $\mu\text{m}$  in the spectrum A2 (more oxidized saponite), suggesting the increasing contribution of  $\text{Fe}^{3+}$  in  $\Sigma\text{Fe}$  due to air exposure [24]. The weak absorption features at 2.40  $\mu\text{m}$  and 2.44  $\mu\text{m}$  in all measurements were attributed to the combination of  $\nu M_n\text{-OH}$  and  $\nu \text{Si-O}$ , which were also observed in the previous studies [24,28].

The strong asymmetric absorption features appeared between 3800–3000  $\text{cm}^{-1}$  wavenumber region in the MIR spectra (Figure 4c). The broad feature was due to vibration of interlayer OH and adsorbed  $\text{H}_2\text{O}$  (hydration) by interlayer cations (3750–3300  $\text{cm}^{-1}$ ), which were overlapped with the peak attributed to the octahedral cation-OH stretching mode around 3600  $\text{cm}^{-1}$ . A sharper feature at 3650  $\text{cm}^{-1}$  in the spectrum A1 than in the spectra B and A2 may be explained by lower contributions of hydration of interlayer cations during the measurements for spectrum A1. The peak position at 3620–3650  $\text{cm}^{-1}$  was distinct from  $\nu \text{Mg}_3\text{-OH}$  of Mg saponite at 3680  $\text{cm}^{-1}$  or  $\nu \text{Fe}^{3+}_2\text{-OH}$  of nontronite at 3570  $\text{cm}^{-1}$ , but they were close to  $\nu \text{Mg}_2\text{Fe}^{2+}\text{-OH}$  of Griffith saponite at 3660  $\text{cm}^{-1}$ . The absorption at 3620  $\text{cm}^{-1}$  was typical for smectites with a high amount of octahedral Al [54]; however, as discussed above, the absence in absorption related to Al at 2.20–2.25  $\mu\text{m}$  suggested that the contribution of octahedral Al was minor. On the other hand, the absorption at 3623  $\text{cm}^{-1}$  of Antwerp talc was assigned to  $\nu \text{Fe}^{2+}_3\text{-OH}$  [51]. Thus, we considered that the observed peak at 3650–3620  $\text{cm}^{-1}$  would be mainly attributed to octahedral  $\text{Fe}^{2+}$ . The change in absorption features at 3800–3000  $\text{cm}^{-1}$  between spectrum A1 and spectra B and A2 would be caused by a difference in the degree of hydration of interlayer cations.

The peak position at 1.40  $\mu\text{m}$  in our ferrous saponite (Figure 4a) was consistent with trioctahedral  $\delta + \nu (\text{Mg}, \text{Fe}^{2+})_3\text{-OH}$  at 1.401  $\mu\text{m}$  of synthesized smectite, sample H, in [27] (high-Mg and low-Al ferrous saponite); however, similar to the absorption features at 3800–3000  $\text{cm}^{-1}$ , the structural OH and  $\text{H}_2\text{O}$  vibrations also caused absorption at  $\sim 1.40$   $\mu\text{m}$  in the NIR spectra. The observed change in absorption depth at around 1.40  $\mu\text{m}$  among the measurements was consistent with the view that different degrees of hydration of interlayer cations, namely, the interlayer cations of samples B and A2, were more hydrated than those of sample A1 (Figure 4c). We also found the appearance of strong absorption at 1.9  $\mu\text{m}$ , attributed to a water molecule in the crystal structure of smectite, for the sample with 50 h of air exposure (Figure A1b). The trend of deeper absorption depths for longer air exposure time was broadly consistent with the change in hydration levels suggested by our XRD analysis. The appearance of 1.9  $\mu\text{m}$  absorption for the unexposed sample was likely to have occurred during the sample preparation in the low- $\text{O}_2$  glovebox, where humidity was around 40%.

The vibrations of tetrahedral Si-O stretching (1200–900  $\text{cm}^{-1}$ ), Si-O bending (600–400  $\text{cm}^{-1}$ ), and octahedral cation-OH bending modes (950–600  $\text{cm}^{-1}$ ) were found in our samples in the MIR range (Figure 4d). The low frequency of the Si-O stretching position around 1000  $\text{cm}^{-1}$  was typical for trioctahedral smectite with low Al contents [55]. The peaks due to Si-O bending mode at 458–444  $\text{cm}^{-1}$  were consistent with Mg saponite

(460  $\text{cm}^{-1}$  and 443  $\text{cm}^{-1}$ ) and Griffith saponite (451  $\text{cm}^{-1}$ ) [51]. The peak positions caused by cation-OH bending mode varied among the spectra B, A1, and A2 (Figure 4d). The peak frequency of 654  $\text{cm}^{-1}$  in spectrum B was slightly lower than that of Mg saponite,  $\delta\text{Mg}_3\text{-OH}$ , 660  $\text{cm}^{-1}$ . In contrast, the frequency increased to 666  $\text{cm}^{-1}$  in spectrum A1. It is empirically known that substitution of dioctahedral Mg into  $\text{Fe}^{2+}$  decreases the vibrational frequency, whereas substitution to  $\text{Fe}^{3+}$  increases the frequency [55]. Assuming that this relationship is applicable to trioctahedral  $\delta\text{Mg}_3\text{-OH}$ , the lower and higher frequencies in the spectra B and A1 were attributed to the presence of octahedral  $\text{Fe}^{2+}$  and  $\text{Fe}^{3+}$ , respectively. The highest absorption peak at 674  $\text{cm}^{-1}$  in spectrum A2 was interpreted as the highest abundance of  $\text{Fe}^{3+}$  in our samples assigned to the Fe–O out-of-plane bending vibration shown in  $\text{Fe}^{3+}$ -bearing smectite around 680  $\text{cm}^{-1}$  [28,51], although this absorption overlapped with octahedral ( $\text{Fe}^{3+}$ , Mg)<sub>3</sub>-OH vibration at 678  $\text{cm}^{-1}$  [51,56]. No absorption associated with  $\delta(\text{Al}, \text{Fe}^{3+})_2\text{-OH}$  in 900–800  $\text{cm}^{-1}$  was observed in all spectra. The absence of absorption around 590–570  $\text{cm}^{-1}$  associated with Fe–O vibration suggested that the contribution of magnetite (or maghemite) was low in the bulk powder samples [57].

## 4. Discussion

### 4.1. Synthesis of Our Analyses

To assess both the adequacy of anaerobic measurements and the impact of air exposure on ferrous saponite, we synthesized the results of our various analyses collected before and after air exposure. Micro XRD patterns exhibited no significant change in structure throughout overnight air exposure, except for interlayer hydration (Figure 1). If the oxidation caused deformation of trioctahedral structure into the dioctahedral structure, the vacant sites of the octahedral sheets could reduce the b unit of the cell parameter, possibly resulting in small 02l and 060 d-space. The constant 02l (4.58 Å) and 060 reflections (1.540 Å) indicated that the structure of ferrous saponite; i.e., a 2:1 layer type with a trioctahedral sheet, was kept throughout the air exposure. By contrast, oxidation of ferrous iron into ferric iron in saponite by air exposure was found based on XANES spectroscopy for both bulk powder and micro STXM analysis (Figures 2 and 3). Our results of STXM analysis showed that oxidation of ferrous saponite occurred heterogeneously at the submicron scale in the Fe-rich area of a saponite particle (Figure 3). Based on our spectral fitting of XAFS spectra of bulk samples,  $\text{Fe}^{3+}/\Sigma\text{Fe}$  of saponite increased from 4% to 15% after 11 h of air exposure (Table 2). The amount of  $\text{Fe}^{3+}/\Sigma\text{Fe}$  in saponite implies that if the structure of saponite changed upon oxidation,  $\text{Fe}^{3+}$ -bearing trioctahedral smectite could be detected in the XRD analysis (c.f., the detectability of mineral phase in XRD: about several percent). Our experimental results suggested that oxidation of Fe in saponite by air exposure did not associate with the structural rearrangement, at least within the air exposure time of 10–18 h.

Previous work demonstrated that oxidation of ferrous saponite by air-saturated water for one week increased the  $\text{Fe}^{3+}/\Sigma\text{Fe}$  ratio from near zero to 24–38% [12]. Although the durations of air or air-saturated water exposure were different between the present study (10–18 h), the relatively high  $\text{Fe}^{3+}/\Sigma\text{Fe}$  (~15%) in our saponite after air exposure suggested that oxidation of ferrous saponite by air proceeded effectively. The previous results using air-saturated water suggested about half of oxidation of ferrous saponite proceeded in the first half-day, implying that the effectivity of oxidation by air may be comparable to those by air-saturated water [12].

Our finding of the occurrence of micro-vein-like Fe(III)-rich structures indicated that oxidation of ferrous saponite proceeded spatially heterogeneously within one ferrous saponite particle (Figure 4i). To identify/evaluate such submicron-scale oxidation, we emphasized the importance of microscopic analysis (such as STXM) for laboratory simulants of water–rock reactions on early Mars and future samples returned from Mars. Given the rapid oxidation of ferrous saponite, our anaerobic treatments during micro XRD measurement, FIB thinning, and sample installation are necessary to avoid an oxidation of ferrous saponite.

The results of our IR spectroscopy were consistent with the results of microscopic X-ray analyses. We found that only small shifts occurred in the absorption position due to cation-OH vibration (Figure 4), supporting that the trioctahedral structure was kept. On the other hand, there were changes in the octahedral cation composition due to air exposure. As described in Section 3.3, the peak frequency due to  $\delta M_3$ -OH vibration in the MIR  $660\text{ cm}^{-1}$  band increased after 14 h of air exposure (Figure 4d). This shift was likely attributed to an increase in  $Fe^{3+}/\Sigma Fe$ , consistent with the results of XANES spectra (Table 2 and Figures 2 and 3). The increasing wavenumber of the  $\nu M_3$ -OH absorption peak (Figure 4c) would reflect the decreasing  $Fe^{2+}$  content in saponite. The previous study showed that an increase in  $\nu + \delta M_3$ -OH absorption at  $2.3\ \mu\text{m}$  can be caused by an increase in  $Fe^{3+}_2$ -OH (or  $Mg_2$ -OH) by oxidation of  $Fe^{2+}$  [28]. Although the shift in the absorption center wavelength toward  $2.3\ \mu\text{m}$  might reflect an increase in the fraction of  $Fe^{3+}$  in saponite, the  $\nu + \delta M_3$ -OH absorption in the NIR range at  $2.3\ \mu\text{m}$  showed no significant shift after 14 h of air exposure (Figure 4b). Our results suggested that the MIR  $660\text{ cm}^{-1}$  band associated with  $\delta(Mg, Fe^{2+}, Fe^{3+})_3$ -OH vibration was more sensitive to iron oxidation of ferrous saponite than the NIR  $2.3\ \mu\text{m}$  band.

#### 4.2. Mechanism for Occurrence of the Fe-Depleted Area in Ferrous Saponite

In the STXM analysis, we found that the Fe-depleted area had low absorption by iron (Figure 3c–f). There are several possibilities that can explain the occurrence of the Fe-depleted area. First, the Fe-depleted area could not be composed of saponite. However, our XRD results of predominance of ferrous saponite, with trace magnetite (or maghemite), in our sample contradict this idea. XRD amorphous components can exist in the sample; nevertheless, it would be difficult to explain depletion of iron in the amorphous phase. Second, there could be a spatial variation in octahedral cation composition; namely, Mg dominated in the Fe-depleted area. However, our STXM measurements at the Mg-K edge for the same sample showed little absorption due to Mg within the Fe-depleted area, whereas the Fe-rich area showed Mg absorption (Appendix B). The measured correlation between Fe and Mg suggests the third possibility; that is, the volume of ferrous saponite had been swollen due to hydration of interlayer cations. Hydration of interlayer cations could have occurred due to humidity in the FIB chamber. To obtain transparent spectra, adjusting the thickness of the sample is essential so that the target element can absorb an irradiated X-ray beam. High levels of moisture adsorption by interlayer of ferrous saponite were confirmed in our XRD patterns, showing the existence of expanding 001 d-space (Figure 1) and IR spectra showing  $H_2O$  absorption bands (Figure 4). If moisture was kept during the STXM measurements, the swollen region in saponite would contain less Fe and other elements. Alternatively, if moisture in saponite was lost during the STXM measurements, the swollen region in saponite would then be shrunk. In either case, the swollen region would become optically thin in the STXM measurements. Therefore, we interpreted the Fe-depleted area to be optically thin because of swelling due to interlayer hydration, and that there would be no mineralogical or chemical difference between the Fe-rich and Fe-depleted areas. We assumed that the extracted XANES spectra at the Fe-rich area reflected ferrous saponite that did not suffer from hydration. We conclude that swelling due to hydration should be considered in preparing FIB thin section samples of ferrous saponite in laboratory simulants, meteorites, and returned samples from Mars and carbonaceous asteroids.

#### 4.3. Mechanism of Ferrous Saponite Oxidation and Its Implications

As discussed in Section 4.1, oxidation of octahedral ferrous iron into ferric iron occurred without any change in the mineralogical structure, at least with 10–18 h of air exposure. The fact that the oxidation of ferrous saponite was observed in our STXM (X-ray transmission) analysis suggested that the oxidation proceeded, at least,  $\sim 0.1\ \mu\text{m}$  in depth from the surface. Given that an IR analysis is sensitive to surface solid materials (in order of  $\mu\text{m}$  in depth from the surface), the results of our bulk IR analysis also suggested that the

oxidation of ferrous iron could have occurred, at most, until a depth of  $\sim 1 \mu\text{m}$ . These results suggested that the oxidation may have proceeded at least  $0.1\text{--}1 \mu\text{m}$  from the surface. This raises a new question; that is, where did excess charge go upon the oxidation of ferrous iron? Since any excess charge should be balanced, electrons can be consumed through substitution of structural  $\text{OH}^-$  by  $\text{O}^{2-}$  [24] or cation migration [12]. Transformation into a dioctahedral structure requires mechanisms to decrease an octahedral site occupancy, which are suggested to occur upon hydrothermal recrystallization and/or effective  $\text{Fe}^{3+}$  ejection by reactions with strong oxidants [12,43]. The iron oxidation associated with the deformation to dioctahedral structure would have a high activation energy and, thus, was likely kinetically inhibited at relatively low temperature (i.e., room temperature  $\sim 20^\circ\text{C}$ ) during air exposure of our sample [12]. In contrast, saponite is characterized by high water adsorption and cation exchangeability within the interlayer structure. This flexibility in the structure could provide the ability to maintain  $\text{Fe}^{3+}$  in a trioctahedral sheet with a low activation energy, allowing the rapid oxidation of octahedral iron at relatively low temperatures. The swollen structure in the Fe-depleted area might enhance the accessibility of interlayer compounds and oxygen in air. This hypothesis may explain that micro-vein-like Fe(III)-rich structures seemed to grow from the boundary between the Fe-rich and Fe-depleted areas (Figure 4i). We hypothesized that volume changes due to partial hydration of saponite could have formed micro-cracks. Upon the air exposure, oxidation of ferrous iron of saponite might have proceeded through the micro-cracks, possibly forming Fe(III)-rich micro-vein-like structures.

The high sensitivity of ferrous saponite to oxidation inferred the possibility of its usage for a promising redox proxy for Martian environments. On early Mars, atmospheric redox states may have dramatically varied over geological time (e.g., [11,58]). In Mars rover missions and Martian meteorite analyses, previous work focused on Mn; e.g., Mn (hydro)oxides, to reconstruct redox states of aqueous environments [3,4,7,10]. With microscopic analyses, ferrous saponite could be an alternative proxy indicator of oxidation on Mars. In fact, through the Mars Sample Return mission, sedimentary rocks at Jezero Crater, where the Mars 2020 Perseverance Rover landed, might be collected and sent to Earth for detailed mineralogical and chemical analyses [30]. Spectroscopic observations suggest the presence of clay minerals, most likely including ferrous saponite, on delta deposits at Jezero Crater [15,30,59]. We suggest that our preparation/measurement methods are applicable to future returned samples from Mars to evaluate in situ oxidation processes. Given the possibility of presence of saponite in returned samples from carbonaceous asteroids, our methods are also applicable to the chemical analysis for the asteroid sample-return missions (Hayabusa 2 and OSIRIS-REx) [37–41].

Another implication of the high sensitivity of ferrous saponite to oxidation is its potential as a reductant to cause redox reactions in natural aqueous environments. The reducing ability of ferrous iron-bearing minerals, such as magnetite and green rust, on early Martian environments has previously been discussed (e.g., [60]). However, knowledge of the reducing ability of ferrous smectite is limited [61]. A continuous supply of reductants is required for chemoautotrophic life on Earth [62] and beyond [63,64]. Estimating the available reductants and their fluxes would also provide insights into the origin of life on early Earth [65–68].

## 5. Conclusions

We conducted microscopic X-ray analyses, bulk XANES, and IR spectroscopy for synthesized ferrous saponite under anaerobic conditions. A comparison between the results before and after air exposure provided the following findings:

- Ferrous saponite was rapidly oxidized by air on an hour to daily timescale at room temperature, at least until  $0.1\text{--}1 \mu\text{m}$  from the surface. Ferric iron replaced octahedral ferrous iron without rearrangement of the trioctahedral structure within this timescale. The oxidation occurred heterogeneously at the submicron scale (micro-vein-like structure) in saponite.

- Our preparation and measurement methods without any air exposure were able to limit oxidation before/during measurements. Avoiding hydration of interlayer cations in saponite is also preferred during FIB thinning of samples for microscopic X-ray analysis, such as STXM.
- Ferrous saponite can be a promising redox indicator for environments on early Mars. Our preparation/measurement methods are applicable to chemical analyses for ferrous saponite in both laboratory simulants and returned extraterrestrial samples.

**Author Contributions:** Conceptualization, Y.T., K.F. and T.N.; methodology, N.N., S.Y., Y.T., M.M., H.S. and T.N.; formal analysis, N.N., Y.E. and K.A.; investigation, N.N., S.Y., M.M., Y.E., K.A. and T.K.; resources, N.N., Y.T. and T.N.; writing—original draft preparation, N.N., S.Y. and K.A.; writing—review and editing, Y.S. and T.N.; visualization, N.N.; project administration, Y.T.; funding acquisition, N.N., Y.T., K.F., Y.S. and T.N. All authors have read and agreed to the published version of the manuscript.

**Funding:** This study was financially supported by KAKENHI JSPS (Grant Nos. JP17H06456, JP17H06458, JP17H06459, JP19J22396, JP20H00188, and JP20H00195).

**Data Availability Statement:** All data generated for Figures 1–4, Figure A1, and Figure A2 are available at <https://figshare.com/s/ac8c70a81a31429b299a>.

**Acknowledgments:** N.N. thanks T. Murakami of Univ. Tokyo for providing equipment. STXM and XRD analyses in this study was performed with the approval of Photon Factory (Nos. 2018S001 and 2020S2-002).

**Conflicts of Interest:** The authors declare no conflict of interest.

## Appendix A

In addition to the NIR diffuse reflectance spectra (Figure 4a,b), VNIR reflectance spectra of synthesized ferrous saponite powder were obtained before and after 12 h of air exposure. Both VNIR reflectance spectra showed absorption peaks due to  $\delta + \nu(\text{Mg, Fe}^{2+})_3\text{-OH}$  at 2.32  $\mu\text{m}$  and 1.40  $\mu\text{m}$  (Figure A1a), similar to our diffuse reflectance NIR spectra (Section 3.3.). The strong absorptions at  $\sim 1.9 \mu\text{m}$  attributed to hydration occurred within the vial used for carrying the sample prior to the measurement (Figure A1b). The air exposure caused darkening in the reflectance spectra at short wavelengths ( $< 1 \mu\text{m}$ ). This trend was also observed in the NIR diffuse reflectance spectra, although the range was almost the measurement limit of the instrument. The darkening of VNIR reflectance spectra by air oxidation was also reported for ferrous saponite with high-Mg and low-Al trioctahedral cation composition (sample D in [12,27]), suggesting the observed darkening in our ferrous saponite sample was also due to the air oxidation.

Figure A1b shows a close-up view of IR absorption features at  $\sim 1.9 \mu\text{m}$  for the air-exposed/unexposed saponite samples. The reflectance NIR spectra of Fe saponite after air exposure for 50 days showed deeper absorption than that obtained before the air exposure. A weak absorption at  $\sim 1.9 \mu\text{m}$  for the sample with 14 h of air exposure (Figure A1b) was consistent with the interpretation of other bands in the FT-MIR/NIR spectra (Section 3.3). The presence of positive shifts in reflectance at around 1.9  $\mu\text{m}$  suggested that the effect of water vapor in the instrument could have been poorly removed. Nevertheless, the absorption due to hydration of the sample with 14 h of air exposure would be weak, even when removing the effect of water vapor.

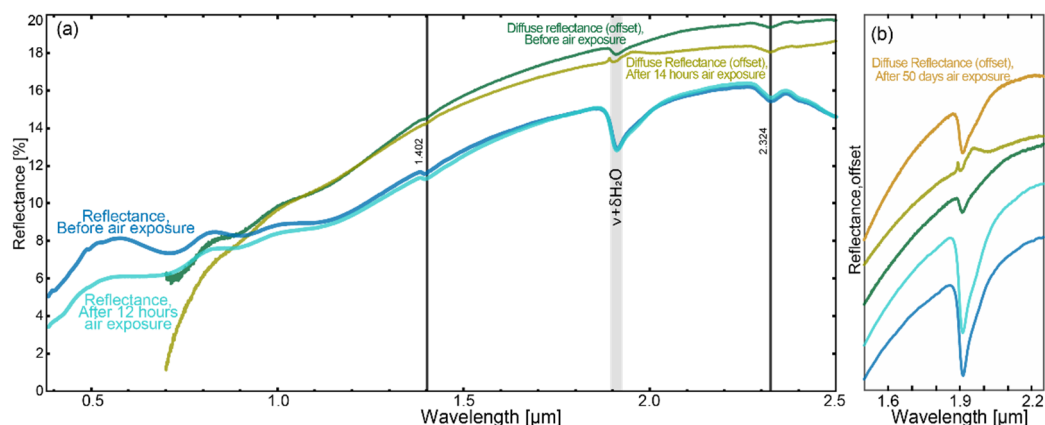


**Figure A1.** (a) Results of VNIR reflectance spectra before and after air exposure for 12 h. The NIR diffuse reflectance spectra are offset and shown for comparison. Note that the continuum components are not removed. Vertical lines show the peak position observed in NIR diffuse reflectance spectra (spectra A1 and B in Figure 4). The solid gray bar shows the position of absorption band due to H<sub>2</sub>O molecules. (b) Close up of a 1.9 μm wavelength region. The colors of the spectra are the same as those in panel (a).

## Appendix B

The additional STXM measurements were performed around the Mg K-edge (1300–1340 eV) following the measurement of the Fe L-edge after air exposure for the same area, pixel size, and dwell time. We found low optical density with little absorption features of Mg in the Fe-depleted area, whereas a relatively high optical density with weak absorption features was found in the Fe-rich area (Figure A2).

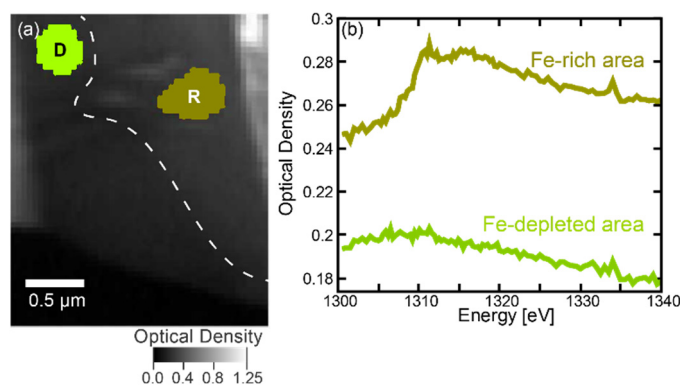


**Figure A2.** Results of XANES mapping by STXM around the Mg K-edge. (a) Raster scanned map at an X-ray energy of 1311.0 eV. Brighter colors represent higher optical densities. The white broken curves represent the approximate borders of the Fe-rich/depleted areas. The areas used for extracting the spectra are shown with the color of the index R (Fe-rich area) and D (Fe-depleted area). (b) The XANES spectra extracted from the Fe-rich/depleted area shown in panel (a).

## References

1. Michalski, J.R.; Cuadros, J.; Niles, P.B.; Parnell, J.; Deanne Rogers, A.; Wright, S.P. Groundwater activity on Mars and implications for a deep biosphere. *Nat. Geosci.* **2013**, *6*, 133–138. [[CrossRef](#)]
2. Michalski, J.R.; Onstott, T.C.; Mojzsis, S.J.; Mustard, J.; Chan, Q.H.S.; Niles, P.B.; Johnson, S.S. The Martian subsurface as a potential window into the origin of life. *Nat. Geosci.* **2018**, *11*, 21–26. [[CrossRef](#)]
3. Arvidson, R.E.; Squyres, S.W.; Morris, R.V.; Knoll, A.H.; Gellert, R.; Clark, B.C.; Catalano, J.G.; Jolliff, B.L.; McLennan, S.M.; Herkenhoff, K.E.; et al. High concentrations of manganese and sulfur in deposits on Murray Ridge, Endeavour Crater, Mars. *Am. Mineral.* **2016**, *101*, 1389–1405. [[CrossRef](#)]

4. Lanza, N.L.; Wiens, R.C.; Arvidson, R.E.; Clark, B.C.; Fischer, W.W.; Gellert, R.; Grotzinger, J.P.; Hurowitz, J.A.; McLennan, S.M.; Morris, R.V.; et al. Oxidation of manganese in an ancient aquifer, Kimberley formation, Gale crater, Mars. *Geophys. Res. Lett.* **2016**, *43*, 7398–7407. [[CrossRef](#)]
5. Hurowitz, J.A.; Fischer, W.W.; Tosca, N.J.; Milliken, R.E. Origin of acidic surface waters and the evolution of atmospheric chemistry on early Mars. *Nat. Geosci.* **2010**, *3*, 323–326. [[CrossRef](#)]
6. Hurowitz, J.A.; Grotzinger, J.P.; Fischer, W.W.; McLennan, S.M.; Milliken, R.E.; Stein, N.; Vasavada, A.R.; Blake, D.F.; Dehouck, E.; Eigenbrode, J.L.; et al. Redox stratification of an ancient lake in Gale crater, Mars. *Science* **2017**, *356*, 1–26. [[CrossRef](#)]
7. Noda, N.; Imamura, S.; Sekine, Y.; Kurisu, M.; Fukushi, K.; Terada, N.; Uesugi, S.; Numako, C.; Takahashi, Y.; Hartmann, J. Highly oxidizing aqueous environments on early Mars inferred from scavenging pattern of trace metals on manganese oxides. *J. Geophys. Res. Planets* **2019**, *124*, 2018JE005892. [[CrossRef](#)]
8. Fukushi, K.; Sekine, Y.; Sakuma, H.; Morida, K.; Wordsworth, R. Semiarid climate and hyposaline lake on early Mars inferred from reconstructed water chemistry at Gale. *Nat. Commun.* **2019**, *10*, 1–11. [[CrossRef](#)]
9. Koike, M.; Nakada, R.; Kajitani, I.; Usui, T.; Tamenori, Y.; Sugahara, H.; Kobayashi, A. In-situ preservation of nitrogen-bearing organics in Noachian Martian carbonates. *Nat. Commun.* **2020**, *11*, 1–7. [[CrossRef](#)]
10. Liu, J.; Michalski, J.R.; Tan, W.; He, H.; Ye, B.; Xiao, L. Anoxic chemical weathering under a reducing greenhouse on early Mars. *Nat. Astron.* **2021**, *5*, 503–509. [[CrossRef](#)]
11. Wordsworth, R.; Knoll, A.H.; Hurowitz, J.; Baum, M.; Ehlmann, B.L.; Head, J.W.; Steakley, K. A coupled model of episodic warming, oxidation and geochemical transitions on early Mars. *Nat. Geosci.* **2021**, *14*, 127–132. [[CrossRef](#)]
12. Chemtob, S.M.; Nickerson, R.D.; Morris, R.V.; Agresti, D.G.; Catalano, J.G. Oxidative Alteration of Ferrous Smectites and Implications for the Redox Evolution of Early Mars. *J. Geophys. Res. Planets* **2017**, *122*, 2469–2488. [[CrossRef](#)] [[PubMed](#)]
13. Rampe, E.B.; Blake, D.F.; Bristow, T.F.; Ming, D.W.; Vaniman, D.T.; Morris, R.V.; Achilles, C.N.; Chipera, S.J.; Morrison, S.M.; Tu, V.M.; et al. Mineralogy and geochemistry of sedimentary rocks and eolian sediments in Gale crater, Mars: A review after six Earth years of exploration with Curiosity. *Chemie Erde* **2020**, *80*, 125605. [[CrossRef](#)]
14. Ehlmann, B.L.; Mustard, J.F.; Murchie, S.L.; Bibring, J.-P.P.; Meunier, A.; Fraeman, A.A.; Langevin, Y. Subsurface water and clay mineral formation during the early history of Mars. *Nature* **2011**, *479*, 53–60. [[CrossRef](#)] [[PubMed](#)]
15. Ehlmann, B.L.; Mustard, J.F.; Fassett, C.I.; Schon, S.C.; Head, J.W.; Des Marais, D.J.; Grant, J.A.; Murchie, S.L. Clay minerals in delta deposits and organic preservation potential on Mars. *Nat. Geosci.* **2008**, *1*, 355–358. [[CrossRef](#)]
16. Mustard, J.F.; Murchie, S.L.; Pelkey, S.M.; Ehlmann, B.L.; Milliken, R.E.; Grant, J.A.; Bibring, J.-P.; Poulet, F.; Bishop, J.; Dobrea, E.N.; et al. Hydrated silicate minerals on Mars observed by the Mars Reconnaissance Orbiter CRISM instrument. *Nature* **2008**, *454*, 305–309. [[CrossRef](#)]
17. Poulet, F.; Bibring, J.-P.; Mustard, J.F.; Gendrin, A.; Mangold, N.; Langevin, Y.; Arvidson, R.E.; Gondet, B.; Gomez, C.; The Omega Team. Phyllosilicates on Mars and implications for early martian climate. *Nature* **2005**, *438*, 623–627. [[CrossRef](#)]
18. Ehlmann, B.L.; Mustard, J.F.; Swayze, G.A.; Clark, R.N.; Bishop, J.L.; Poulet, F.; Des Marais, D.J.; Roach, L.H.; Milliken, R.E.; Wray, J.J.; et al. Identification of hydrated silicate minerals on Mars using MRO-CRISM: Geologic context near Nili Fossae and implications for aqueous alteration. *J. Geophys. Res.* **2009**, *114*, E00D08. [[CrossRef](#)]
19. Ehlmann, B.L.; Edwards, C.S. Mineralogy of the Martian Surface. *Annu. Rev. Earth Planet. Sci.* **2014**, *42*, 291–315. [[CrossRef](#)]
20. Michalski, J.R.; Cuadros, J.; Bishop, J.L.; Darby Dyar, M.; Dekov, V.; Fiore, S. Constraints on the crystal-chemistry of Fe/Mg-rich smectitic clays on Mars and links to global alteration trends. *Earth Planet. Sci. Lett.* **2015**, *427*, 215–225. [[CrossRef](#)]
21. Catalano, J.G. Thermodynamic and mass balance constraints on iron-bearing phyllosilicate formation and alteration pathways on early Mars. *J. Geophys. Res. E Planets* **2013**, *118*, 2124–2136. [[CrossRef](#)]
22. Cannon, K.M.; Parman, S.W.; Mustard, J.F. Primordial clays on Mars formed beneath a steam or supercritical atmosphere. *Nature* **2017**, *552*, 88–91. [[CrossRef](#)] [[PubMed](#)]
23. Vaniman, D.T.; Bish, D.L.; Ming, D.W.; Bristow, T.F.; Morris, R.V.; Blake, D.F.; Chipera, S.J.; Morrison, S.M.; Treiman, A.H.; Rampe, E.B.; et al. Mineralogy of a mudstone at Yellowknife Bay, Gale crater, Mars. *Science* **2014**, *343*, 1243480. [[CrossRef](#)] [[PubMed](#)]
24. Treiman, A.H.; Morris, R.V.; Agresti, D.G.; Graff, T.G.; Achilles, C.N.; Rampe, E.B.; Bristow, T.F.; Blake, D.F.; Vaniman, D.T.; Bish, D.L.; et al. Ferrian saponite from the Santa Monica Mountains (California, U.S.A., Earth): Characterization as an analog for clay minerals on Mars with application to Yellowknife Bay in Gale Crater. *Am. Mineral.* **2014**, *99*, 2234–2250. [[CrossRef](#)]
25. Kohyama, N.; Shimoda, S.; Sudo, T. Iron-rich saponite (ferrous and ferric forms). *Clays Clay Miner.* **1973**, *21*, 229–237. [[CrossRef](#)]
26. Badaut, D.; Besson, G.; Decarreau, A.; Rautureau, R. Occurrence of a ferrous, trioctahedral smectite in Recent sediments of Atlantis II Deep, Red Sea. *Clay Miner.* **1985**, *20*, 389–404. [[CrossRef](#)]
27. Chemtob, S.M.; Nickerson, R.D.; Morris, R.V.; Agresti, D.G.; Catalano, J.G. Synthesis and structural characterization of ferrous trioctahedral smectites: Implications for clay mineral genesis and detectability on Mars. *J. Geophys. Res. Planets* **2015**, *120*, 1119–1140. [[CrossRef](#)]
28. Fox, V.K.; Kupper, R.J.; Ehlmann, B.L.; Catalano, J.G.; Razzell-Hollis, J.; Abbey, W.J.; Schild, D.J.; Nickerson, R.D.; Peters, J.C.; Katz, S.M.; et al. Synthesis and characterization of Fe(III)-Fe(II)-Mg-Al smectite solid solutions and implications for planetary science. *Am. Mineral.* **2021**, *106*, 964–982. [[CrossRef](#)]
29. Sakuma, H.; Morida, K.; Takahashi, Y.; Fukushi, K.; Noda, N.; Sekine, Y.; Tamura, K. Synthesis of Ferrian and Ferro-Saponites: Implications for the structure of (Fe,Mg)-smectites synthesized in reduced conditions. *Am. Mineral.* **2022**, in press. [[CrossRef](#)]

30. Farley, K.A.; Williford, K.H.; Stack, K.M.; Bhartia, R.; Chen, A.; de la Torre, M.; Hand, K.; Goreva, Y.; Herd, C.D.K.; Hueso, R.; et al. Mars 2020 Mission Overview. *Space Sci. Rev.* **2020**, *216*, 1–41. [[CrossRef](#)]
31. Usui, T.; Bajo, K.-i.; Fujiya, W.; Furukawa, Y.; Koike, M.; Miura, Y.N.; Sugahara, H.; Tachibana, S.; Takano, Y.; Kuramoto, K. The Importance of Phobos Sample Return for Understanding the Mars-Moon System. *Space Sci. Rev.* **2020**, *216*, 1–18. [[CrossRef](#)]
32. De Sanctis, M.C.; Ammannito, E.; Raponi, A.; Marchi, S.; McCord, T.B.; McSween, H.Y.; Capaccioni, F.; Capria, M.T.; Carrozzo, F.G.; Ciarniello, M.; et al. Ammoniated phyllosilicates with a likely outer Solar System origin on (1) Ceres. *Nature* **2015**, *528*, 241–244. [[CrossRef](#)] [[PubMed](#)]
33. De Sanctis, M.C.; Raponi, A.; Ammannito, E.; Ciarniello, M.; Toplis, M.J.; McSween, H.Y.; Castillo-Rogez, J.C.; Ehlmann, B.L.; Carrozzo, F.G.; Marchi, S.; et al. Bright carbonate deposits as evidence of aqueous alteration on (1) Ceres. *Nature* **2016**, *536*, 54–57. [[CrossRef](#)] [[PubMed](#)]
34. De Sanctis, M.C.; Ammannito, E.; Raponi, A.; Frigeri, A.; Ferrari, M.; Carrozzo, F.G.; Ciarniello, M.; Formisano, M.; Rousseau, B.; Tosi, F.; et al. Fresh emplacement of hydrated sodium chloride on Ceres from ascending salty fluids. *Nat. Astron.* **2020**, *4*, 786–793. [[CrossRef](#)]
35. Sekine, Y.; Shibuya, T.; Postberg, F.; Hsu, H.-W.; Suzuki, K.; Masaki, Y.; Kuwatani, T.; Mori, M.; Hong, P.K.; Yoshizaki, M.; et al. High-temperature water–rock interactions and hydrothermal environments in the chondrite-like core of Enceladus. *Nat. Commun.* **2015**, *6*, 8604. [[CrossRef](#)] [[PubMed](#)]
36. Ammannito, E.; Desanctis, M.C.; Ciarniello, M.; Frigeri, A.; Carrozzo, F.G.; Combe, J.P.; Ehlmann, B.L.; Marchi, S.; McSween, H.Y.; Raponi, A.; et al. Distribution of phyllosilicates on the surface of Ceres. *Science* **2016**, *353*. [[CrossRef](#)]
37. Hamilton, V.E.; Simon, A.A.; Christensen, P.R.; Reuter, D.C.; Clark, B.E.; Barucci, M.A.; Bowles, N.E.; Boynton, W.V.; Brucato, J.R.; Cloutis, E.A.; et al. Evidence for widespread hydrated minerals on asteroid (101955) Bennu. *Nat. Astron.* **2019**, *3*, 332–340. [[CrossRef](#)]
38. Kitazato, K.; Milliken, R.E.; Iwata, T.; Abe, M.; Ohtake, M.; Matsuura, S.; Arai, T.; Nakauchi, Y.; Nakamura, T.; Matsuoka, M.; et al. The surface composition of asteroid 162173 Ryugu from Hayabusa2 near-infrared spectroscopy. *Science* **2019**, *364*, 272–275. [[CrossRef](#)]
39. Lauretta, D.S.; Balram-Knutson, S.S.; Beshore, E.; Boynton, W.V.; Drouet d’Aubigny, C.; DellaGiustina, D.N.; Enos, H.L.; Golish, D.R.; Hergenrother, C.W.; Howell, E.S.; et al. OSIRIS-REx: Sample Return from Asteroid (101955) Bennu. *Space Sci. Rev.* **2017**, *212*, 925–984. [[CrossRef](#)]
40. Watanabe, S.; Tsuda, Y.; Yoshikawa, M.; Tanaka, S.; Saiki, T.; Nakazawa, S. Hayabusa2 Mission Overview. *Space Sci. Rev.* **2017**, *208*, 3–16. [[CrossRef](#)]
41. Watanabe, S.; Hirabayashi, M.; Hirata, N.; Hirata, N.; Noguchi, R.; Shimaki, Y.; Ikeda, H.; Tatsumi, E.; Yoshikawa, M.; Kikuchi, S.; et al. Hayabusa2 arrives at the carbonaceous asteroid 162173 Ryugu—A spinning top-shaped rubble pile. *Science* **2019**, *364*, 268–272. [[CrossRef](#)] [[PubMed](#)]
42. Kebukawa, Y.; Okudaira, K.; Yabuta, H.; Hasegawa, S.; Tabata, M.; Furukawa, Y.; Ito, M.; Nakato, A.; Kilcoyne, A.L.D.; Kobayashi, K.; et al. STXM-XANES analyses of Murchison meteorite samples captured by aerogel after hypervelocity impacts: A potential implication of organic matter degradation for micrometeoroid collection experiments. *Geochem. J.* **2019**, *53*, 53–67. [[CrossRef](#)]
43. Decarreau, A.; Bonnin, D. Synthesis and crystallogenesi s at low temperature of Fe(III)-smectites by evolution of coprecipitated gels: Experiments in partially reducing conditions. *Clay Miner.* **1986**, *21*, 861–877. [[CrossRef](#)]
44. Baldermann, A.; Dohrmann, R.; Kaufhold, S.; Nickel, C.; Letofsky-Papst, I.; Dietzel, M. The Fe-Mg-saponite solid solution series – a hydrothermal synthesis study. *Clay Miner.* **2014**, *49*, 391–415. [[CrossRef](#)]
45. Kanzaki, Y.; Murakami, T. Estimates of atmospheric CO<sub>2</sub> in the Neoproterozoic from paleosols. *Geochim. Cosmochim. Acta* **2015**, *159*, 190–219. [[CrossRef](#)]
46. Tabata, H.; Sekine, Y.; Kanzaki, Y.; Sugita, S. An experimental study of photo-oxidation of Fe(II): Implications for the formation of Fe(III) (hydro)oxides on early Mars and Earth. *Geochim. Cosmochim. Acta* **2021**, *299*, 35–51. [[CrossRef](#)]
47. Takeichi, Y.; Inami, N.; Suga, H.; Miyamoto, C.; Ueno, T.; Mase, K.; Takahashi, Y.; Ono, K. Design and performance of a compact scanning transmission X-ray microscope at the Photon Factory. *Rev. Sci. Instrum.* **2016**, *87*, 013704. [[CrossRef](#)]
48. Hitchcock, A.P. aXis 2000—Analysis of X-ray Images and Spectra. Available online: <http://unicorn.mcmaster.ca/aXis2000.html> (accessed on 5 November 2021).
49. Ito, M.; Okamoto, M.; Shibata, M.; Sasaki, Y.; Danhara, T.; Suzuki, K.; Watanabe, T. Mineral Composition Analysis of Bentonite. *PNC Tech. Rep.* **1993**, *36*, 1–119.
50. Ravel, B.; Newville, M. ATHENA, ARTEMIS, HEPHAESTUS: Data analysis for X-ray absorption spectroscopy using IFEFFIT. *J. Synchrotron Radiat.* **2005**, *12*, 537–541. [[CrossRef](#)]
51. Madejová, J.; Gates, W.P.; Petit, S. IR Spectra of Clay Minerals. In *Infrared and Raman Spectroscopies of Clay Minerals*; Elsevier: Amsterdam, The Netherlands, 2017; Volume 8, pp. 107–149. [[CrossRef](#)]
52. Morodome, S.; Kawamura, K. Swelling behavior of Na- and Ca-montmorillonite up to 150 °C by in situ x-ray diffraction experiments. *Clays Clay Miner.* **2009**, *57*, 150–160. [[CrossRef](#)]
53. Bristow, T.F.; Rampe, E.B.; Achilles, C.N.; Blake, D.F.; Chipera, S.J.; Craig, P.; Crisp, J.A.; Des Marais, D.J.D.J.; Downs, R.T.; Gellert, R.; et al. Clay mineral diversity and abundance in sedimentary rocks of Gale crater, Mars. *Sci. Adv.* **2018**, *4*, eaar3330. [[CrossRef](#)] [[PubMed](#)]
54. Madejová, J. FTIR techniques in clay mineral studies. *Vib. Spectrosc.* **2003**, *31*, 1–10. [[CrossRef](#)]

55. Gates, W.P.; Petit, S.; Madejová, J. Applications of NIR/MIR to Determine Site Occupancy in Smectites. *Dev. Clay Sci.* **2017**, *8*, 200–221. [[CrossRef](#)]
56. Komadel, P.; Madejová, J.; Laird, D.A.; Xia, Y.; Stucki, J.W. Reduction of Fe(III) in griffithite. *Clay Miner.* **2000**, *35*, 625–634. [[CrossRef](#)]
57. Lane, M.D.; Bishop, J.L. Mid-infrared (Thermal) Emission and Reflectance Spectroscopy. *Remote Compos. Anal.* **2019**, 42–67. [[CrossRef](#)]
58. Koyama, S.; Terada, N.; Nakagawa, H.; Kuroda, T.; Sekine, Y. Stability of Atmospheric Redox States of Early Mars Inferred from Time Response of the Regulation of H and O Losses. *Astrophys. J.* **2021**, *912*, 135. [[CrossRef](#)]
59. Goudge, T.A.; Milliken, R.E.; Head, J.W.; Mustard, J.F.; Fassett, C.I. Sedimentological evidence for a deltaic origin of the western fan deposit in Jezero crater, Mars and implications for future exploration. *Earth Planet. Sci. Lett.* **2017**, *458*, 357–365. [[CrossRef](#)]
60. Tosca, N.J.; Ahmed, I.A.M.M.; Tutolo, B.M.; Ashpitel, A.; Hurowitz, J.A. Magnetite authigenesis and the warming of early Mars. *Nat. Geosci.* **2018**, *11*, 635–639. [[CrossRef](#)]
61. O'Loughlin, E.J.; Boyanov, M.I.; Kemner, K.M.; Thalhhammer, K.O. Reduction of Hg(II) by Fe(II)-Bearing Smectite Clay Minerals. *Minerals* **2020**, *10*, 1079. [[CrossRef](#)]
62. Amend, J.P.; McCollom, T.M.; Hentscher, M.; Bach, W. Catabolic and anabolic energy for chemolithoautotrophs in deep-sea hydrothermal systems hosted in different rock types. *Geochim. Cosmochim. Acta* **2011**, *75*, 5736–5748. [[CrossRef](#)]
63. Hoehler, T.M. An Energy Balance Concept for Habitability. *Astrobiology* **2007**, *7*, 824–838. [[CrossRef](#)] [[PubMed](#)]
64. Sekine, Y. Habitability and Planetary Redox. *Viva Origino* **2020**, *48*, 6. [[CrossRef](#)]
65. Russell, M.J.; Hall, A.J. The emergence of life from iron monosulphide bubbles at a submarine hydrothermal redox and pH front. *J. Geol. Soc. London.* **1997**, *154*, 377–402. [[CrossRef](#)] [[PubMed](#)]
66. Martin, W.; Baross, J.; Kelley, D.; Russell, M.J. Hydrothermal vents and the origin of life. *Nat. Rev. Microbiol.* **2008**, *6*, 805–814. [[CrossRef](#)] [[PubMed](#)]
67. Martin, W.F. Hydrogen, metals, bifurcating electrons, and proton gradients: The early evolution of biological energy conservation. *FEBS Lett.* **2012**, *586*, 485–493. [[CrossRef](#)]
68. Barge, L.M.; Branscomb, E.; Brucato, J.R.; Cardoso, S.S.S.; Cartwright, J.H.E.; Danielache, S.O.; Galante, D.; Kee, T.P.; Miguel, Y.; Mojzsis, S.; et al. Thermodynamics, Disequilibrium, Evolution: Far-From-Equilibrium Geological and Chemical Considerations for Origin-Of-Life Research. *Orig. Life Evol. Biosph.* **2017**, *47*, 39–56. [[CrossRef](#)]